https://dx.doi.org/10.1016/j.jpowsour.2021.230179

Understanding potassium ion storage mechanism in pitch-derived soft carbon and the consequence on cyclic stability

Hong Tan, Rui Zhou, Biao Zhang *

Department of Applied Physics, the Hong Kong Polytechnic University, Hung Hom, Hong Kong, P.R. China. Email: biao.ap.zhang@polyu.edu.hk

Abstract

Carbon materials are considered the most promising anodes for emerging potassium ion batteries. While hard carbon has shown attractive capacities, soft carbon possesses advantages in the tap density for obtaining high volumetric energy density. Systematic studies are conducted in this work to explore the potential active sites for K ion storage and the associated stability upon repeated K ion insertion/extraction. Pitch-derived soft carbon is utilized as a model material due to its high carbon purity so that the interference of heteroatoms could be minimized. Stepwise carbonization is performed to gradually tune the degree of order, allowing the establishment of the correlation between the charge storage mechanism and microstructure by *in situ* Raman spectroscopy. *Ex situ* TEM images of the electrodes after cycles are collected to examine the likely structural deterioration upon the insertion of relative large K ions. The kinetics of charge transfer in various active sites are exploited to achieve a holistic performance in both the energy and power densities. This work unravels the structure-dependent potassium storage behaviors in soft carbon and would benefit the optimization of microstructure for designing advanced anodes.

Keywords: pitch; soft carbon; in-situ Raman; potassium ion batteries

1. Introduction

The hopes of potassium-ion batteries (PIBs) revived after over 80 years of silence. The benefits of the research on PIBs are twofold. On the one hand, it would provide an alternative energy storage device at a relatively low cost for stationary energy application. Concerns on the scarcity of lithium for the upcoming electrification era rise recently, complementary PIBs, if successfully developed, could partly release the stress. On the other hand, shifting from Li to K ion systems would enhance our fundamental understanding of the intercalation chemistry, which will in turn boost the development of Li-ion batteries (LIBs). Recent progress on PIBs takes full advantage of the knowledge accumulated in LIBs thanks to the similarity between alkali metal ion insertion [1–6]. Several cathodes material, analogous to their counterparts in LIBs, have been designed, such as layered oxide $K_{0.3}MnO_2$ [7], Prussian blue $K_xMnFe(CN_6)$ [8] and polyanionic compounds $K_3V_2(PO_4)_2F_3$ [9], $KVPO_4F$ [10]. These cathodes deliver promising capacities and stability during K ion uptake and extraction, indicating the large radius of K ion is not an insurmountable obstacle for designing host materials.

Turn to the anodes, the mainstream of research originally follows the way paved by graphite due to its success in LIBs, focusing either on stabilization of the graphite anode by modification of electrolyte [11,12] and binder [13] or on the investigation of different types of graphitic materials [14,15]. Meanwhile, research interest gradually covers a wider range of materials including disordered carbon, heteroatom-doped carbon[16–18], insertion-type MoS_2 [19] and alloying-type Sb [20], Bi [21]. Among them, disordered carbon holds great application prospects due to its large abundance, facile manufacturing process, and decent capacity. Depending on its graphitizability, disordered carbon can be classified as hard (non-graphitizable) and soft (graphitizable) carbon, which stems from the nature of the starting precursors [22]. A certain amount

of nanopores is presented in the hard carbon, which largely accommodates the volume expansion and improves the durability upon long-term cycles. The presence of pores, however, would reduce the tap density of the electrode, resulting in low volumetric energy density.

As another important type of disordered carbon, soft carbon shows relatively high density with the exclusion of pores, making it attractive for high volumetric energy density batteries. Early works have shown that soft carbon has better rate capability over traditional graphite and hard carbon [23–25]. In terms of its cycling stability, discrepancy exists due possibly to the difference in precursors and variation of fabrication methods [26–28], which both have large impacts on the evolution of carbon structures and the resulting electrochemical performances. Due to its graphitizable nature, soft carbon usually contains a certain amount of ordered structure, which may help improve the electrochemical performance by enhancing its structural flexibility [29,30]. However, the clear correlation between the degree of order for soft carbon and corresponding potassium ion storage remains elusive. Herein, we synthesized a series of soft carbon with regularly-tuned microstructure by stepwise annealing of mesophase pitch from 800 to 2800 ℃. The K ion storage sites in soft carbon and relevant stability were thus investigated using the as-prepared materials. Choosing pitch as the starting material is based on the following two considerations. First, the pitch is an abundant compound available from both natural deposits and petroleum industry. The low cost and high carbon yield make it a promising research candidate towards practical applications. Second, the pitch has a low content of impurities, which enables us to explore the potential potassium ion active sites in neat carbon with minor interference of heteroatoms.

2. Experimental

2.1 Material preparation and characterization

Soft carbon materials were prepared via a two-step carbonization process from the mesophase pitch. The precursor was first stabilized in the air at 300 ℃ for 4h in a muffle furnace. After grinding in an agate mortar, the mildly carbonized powder was then fully carbonized in Ar at target temperatures (800 ℃, 1400 ℃, 2000 ℃, 2800 ℃) for 2h with a ramping rate of 5 ℃ min^{-1}. Medium temperature heat treatment (800 ℃, 1400 ℃) was conducted in a tube furnace while high-temperature ones (2000 ℃, 2800 ℃) were carried out in a graphite furnace. The products were directly collected afterward without any post-treatment and named after their heat treatment temperature as SC-800, SC-1400, SC-2000, and SC-2800. The corresponding carbon yield is 77%, 69%, 56% and 52%, respectively (Table. S1). The morphologies of the samples were characterized by scanning electron microscopy (SEM, JEOL-6490) and transmission electron microscopy (TEM, JEOL 2010F). Carbon structure was investigated using X-ray diffraction (XRD, Rigaku Smart Lab) and Raman spectroscopy (Witec-Confocal Raman system (UHTS 600 SMFC VIS)). The elemental composition was determined by X-ray photoelectron spectroscopy (XPS, PHI5600, Physical Electronics, Inc.). Pore structure was analyzed using N_2 adsorption/desorption isotherms obtained on a micromeritics ASAP 2020 machine.

2.2 Characterizations

The electrodes comprise 80 wt.% active material, 10wt.% conductive carbon black, and 10wt.% carboxymethylcellulose sodium binder. The mixtures were dispersed and stirred in de-ionized water to form a homogeneous slurry, which was coated on a copper foil for making the electrode tape. Discs with a diameter of 12 mm were cut from the tape to employ as working electrodes in the SC//K half cells. The typical loading of each electrode was around 2.0 mg. Standard CR2032 coin cells were

then assembled in an argon-filled glove box with oxygen and water content lower than 0.5 ppm. 0.8 M KPF_6 in ethylene carbonate (EC)/dimethyl carbonate (DEC) (1:1 in volume) was initially used as the electrolyte and 1.0 M KFSI in ethylene glycol diethyl ether (EGDE, Macklin) was adopted as a referenced one. A piece of glass fiber (Whatman, GF/D) was applied as a separator. Typically, 80 μL of the electrolyte was added to each cell. The electrochemical performance of the cells was tested by the galvanostatic cycling method on LAND CT2001A Battery Testing systems. The profiles by galvanostatic intermittent titration technique (GITT) were collected on Arbin battery testing systems.

For the in-situ Raman test, the pure soft carbon was used to eliminate the effect of carbon black and binders. A lens with a working distance of 9 mm was used in the Witec confocal Raman system. Optical pictures were collected synchronously during the test. The characterization of cycled materials was carried out using the electrodes after 100 cycles. For the post-cycle TEM test, the carbon materials were scratched off from the electrodes and soaked in dimethyl carbonate (DMC) in a glovebox. After vigorous shaking, the supernatant liquor was collected for the sample preparation in the glovebox.

3. Results and discussion

3.1 Structure investigation of soft carbon

The obtained soft carbon mainly exhibits bulk-like morphology, while the SC-2800 shows a layer-like feature on the fracture surface (Fig. S1). TEM images (Fig. 1a-d) demonstrate the typical turbostratic structures in SC-800 and SC-1400. In contrast, the graphene layers start to grow in a parallel manner in SC-2000 and finally turn into a characteristic graphitic feature in SC-2800 with straight graphene layers aligned by a fixed interlayer distance. The interlayer spacings of the samples show a gradual narrow-

down from 3.56 Å to 3.37 Å when annealing temperature increases from 800 ℃ to 2800 ℃ (Fig. 1e). The value of SC-2800 is very close to that of natural graphite (3.35 Å). It is worth noting that large proportions of disordered domains remain in the SC-2800. Fully graphitization requires longer holding time, external pressure, and even higher temperature during graphitization. Raman spectra (Fig. 1f) further reveal that the degree of disorder decreases along with the reduction of defects under increasing calcination temperature. The I_D/I_G ratio of the sample drops from 0.98 for SC-800 to 0.84, 0.35, 0.05 for SC-1400, SC-2000 and SC-2800, respectively. Meanwhile, along with the intensifying of G band and the shrink of D band in the spectra for SC-2000 and SC-2800, the 2D band also appears as an indicator of the augment of the number of stacked graphene layers. As a result, SC-2800 shows the highest crystallinity (L_c) of 524 Å and the largest in-plane graphene length (L_a) of 38 nm (Table. S2) [31]. Furthermore, the degree of graphitization (DOG) of the sample is estimated to be 0.02, 0.07, 0.5 and 0.81 for SC-800, SC-1400, SC-2000 and SC-2800, separately, by integrating the methods by Maire et al. [32] and Aune et al. [33] (details elucidated in Table. S3.).

Unlike hard carbon, which usually contains a certain amount of impurities, soft carbon comprises only carbon and minor oxygen (Table. S4). The carbon content has a high value of 96.1% even under a low carbonization temperature of 800 ℃ and increases to over 99% with an annealing temperature above 2000 ℃ (Fig. S2). Along with the increase of temperature from 800 to 2800 ℃, the amount of Sp^3 C-C species drops from 24.3% to 19% while the content of in-plane Sp^2 C=C species increases from 56.2% to 69.2% (Table. S5). It indicates the continuous growth of graphitic layers and agrees well with XRD and Raman results. Concurrent with the graphitization process, the surface area of the sample by Brunauer-Emmett-Teller (BET) method (Fig. S3,

Table. S6) is slightly decreased from 3.45 $m^2 \cdot g^{-1}$ for SC-800 to 1.83, 0.89 and 082 $m^2 \cdot g^{-1}$ for SC-1400, SC-2000 and SC-2800, separately. The reason lies in the densification during the high-temperature treatment, which is consistent with the decrease in the carbon yield. The surface area is quite small compared to that of hard carbon, which has a value of tens of times higher. Thus, the capacity contribution from charge storage in the nanopores is normally considered negligible in soft carbon.

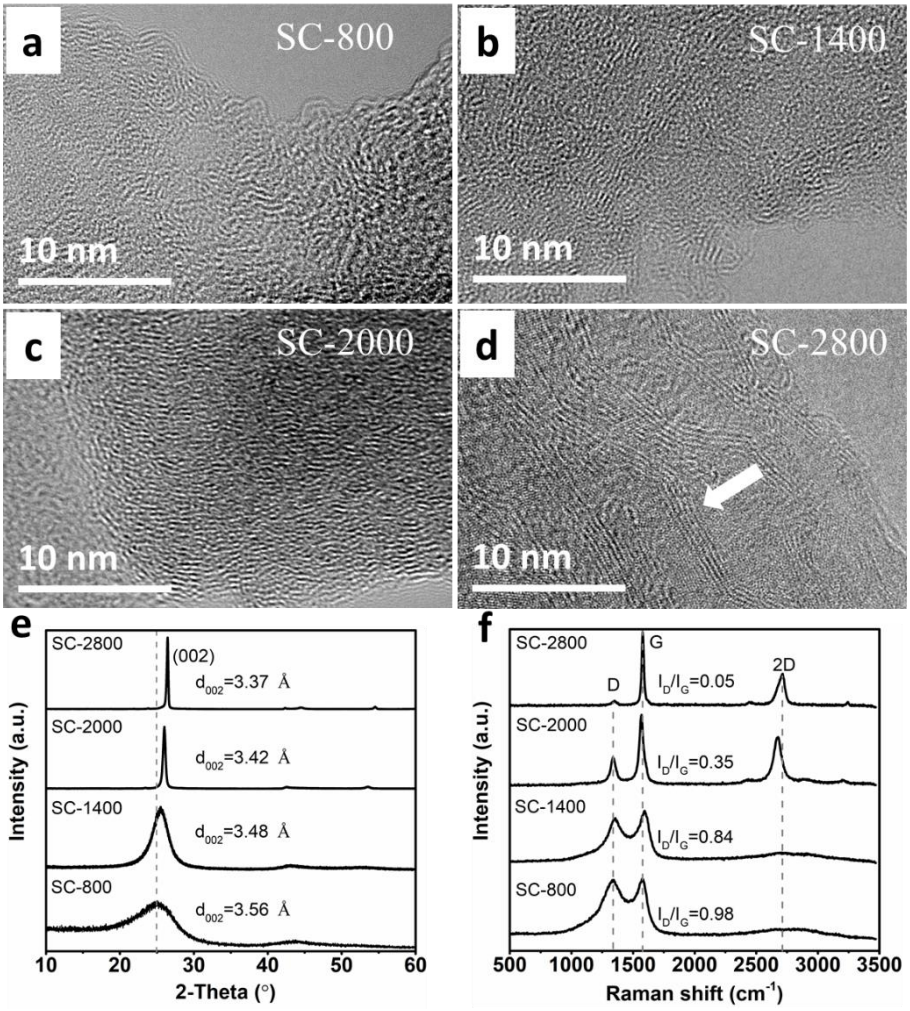

Fig. 1. TEM images of (a) SC-800, (b) SC-1400, (c) SC-2000, (d) SC-2800; (e) XRD patterns and (f) Raman spectra for SC-800, SC-1400, SC-2000 and SC-2800.

3.2 Potassium storage mechanisms in soft carbon

The voltage profiles of soft carbon in Fig.2a show a gradual down-shift of average charge-discharge potential with the treated temperature rising from 800 to 2800 °C.

Meanwhile, the voltages profiles also exhibit a mild slope-plateau combined feature, with the slope and plateau regions corresponding to the dQ/dV peaks located at high and low potentials, respectively, indicating that different charge storage behaviors were involved (Fig. 2b). According to the potentials of plateau indicated by dQ/dV curves, a subline was drawn in each voltage profile to separate the charge contribution from different storage sites. The results showed that the plateau-related capacity contribution (below subline) increases from 9% for SC-800, to 29% for SC-1400 and to around 50% for both SC-2000 and SC-2800 (Fig. 2c).

Being sensitive for detecting the intercalation process for disorder and poor graphitized carbon materials, the *in situ* Raman was carried out to explore the charge storage mechanisms associated with the sloping and plateau regions. As shown in Fig. 3a, the D- and G-band of SC-800 appears initially at 1330 cm^{-1} and 1593 cm^{-1}. Upon the subsequent discharge and charge, neither apparent peak shift nor I_D/I_G change can be observed, which implies that the negligible intercalation process is involved. The phenomenon is similar to the one found in low-temperature treated hard carbon, where adsorption of K ions on tiny graphene layers and in defects is the primary mechanism accounting for the capacity [34]. Different from SC-800, the D- and G- band of SC-1400 (Fig. 3b) slightly shift from 1345 cm^{-1} and 1593 cm^{-1} to 1330 cm^{-1} and 1579 cm^{-1}, respectively, upon 1st discharge to 0.18 V. The peaks are finally diminished at 0 V, transforming into a bump-like shape accompanied with an evident shift to lower wavenumber, which suggests the formation of low-stage graphite-intercalation-compounds (GICs). The result is also confirmed by the *in situ* XRD (Fig. S4).

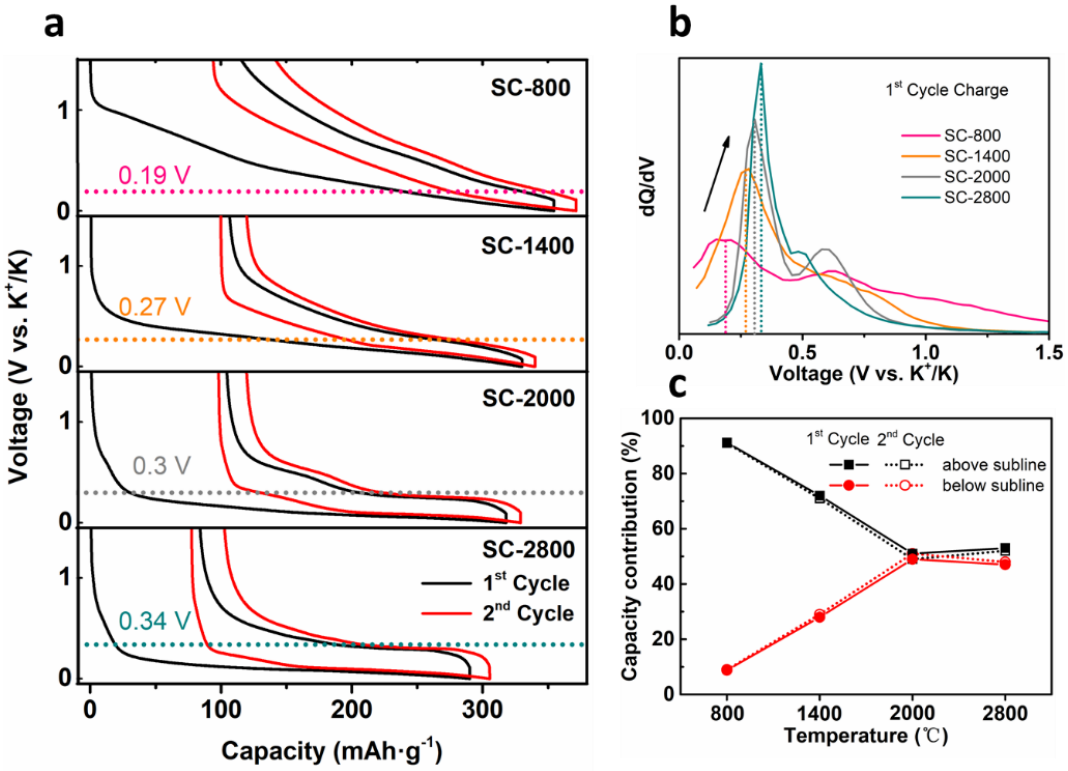

Fig. 2. (a) Voltage profiles, (b) dQ/dV curves and (c) capacity contribution above/below subline for SC-800, SC-1400, SC-2000 and SC-2800.

For SC-2000 containing a large proportion of graphitic structure (Fig. 3c), the signal of D- and 2D-band vanishes when discharged to 0.25 V, along with the blue-shift of G-band from 1579 cm^{-1} to 1602 cm^{-1}. Since D-band reflects the presence of defects and edges of graphene layers, the fading of its signal could result from the occupying of the limited defect sites by K ions. The weakening of 2D-band could be attributed to the shielding effect of the intensified vibration of the external charged graphene layers upon K intercalation on the inner double resonance [35]. The initial blue-shift of G-line stems from the charge transfer from potassium to the graphene layers, while the subsequent slight red-shift (denoted by the dashed line) can be ascribed to the increasing of C-C band length and internal strain brought about by the intercalation of K ions [36]. Although SC-2000 is partly graphitized, it fails to proceed with the identifiable staging reactions, thus no doublet tranformation is detectable for

G-band. Despite that, the asymmetric fano-resonance shaped line at 0 V gives evidence to the formation of stage I GICs [37].

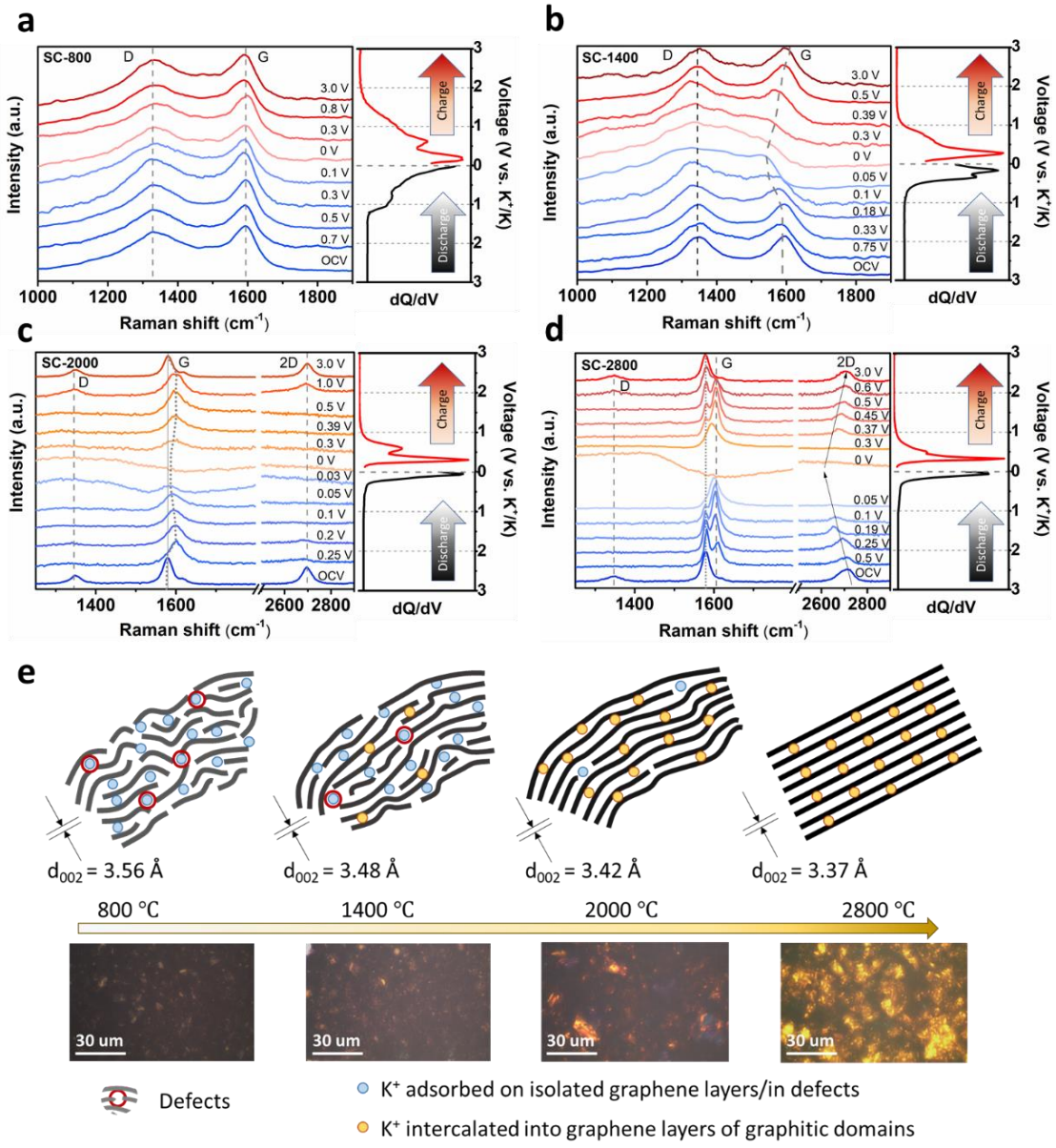

Fig. 3. In-situ Raman spectra with corresponding dQ/dV curves upon the 1st cycle charge and discharge process for (a) SC-800; (b) SC-1400; (c) SC-2000; (d) SC-2800. (e)Schematic illustration of the microstructure evolution of soft carbon derived under different annealing temperatures and the corresponding K^+ storage behaviors. The optical image shows the color of samples discharged to 0V.

Although the intercalation could be detected in both SC-1400 and SC-2000, the

GICs formation does not follow the pathways observed previously in graphite due to the poor graphitization degree. A sharp contrast is observed in highly graphitic SC-2800. The emerging of large graphitic domains allows the strict staging reactions to take place, as demonstrated by the clear and highly reversible evolution of G- and 2D-band (Fig. 3d). Upon discharge to 0.25V, the G-band splits into two sub-peaks, namely the E_{2g2}(i) at 1582 cm^{-1} and E_{2g2}(b) at 1610 cm^{-1}, representing the uncharged graphene layers (G_{UC}) and charged graphene layers (G_C), respectively [38]. Following the discharge process to 0 V, a full reaction course was recorded (Fig. S5): KC_{72} (stage VI) → KC_{60} (stage VI) → KC_{48} (stage VI) → KC_{36} (stage III) → KC_{24}/KC_{16} (stage II) →KC_8 (stage I), where KC_{16} emerges as a transition phase as indicated by Liu et al. [39]. It suggests that the graphitized soft carbon shares the same K ion intercalation mechanism with natural graphite [40]. Besides, a series of real-time optical images were taken during the in-situ Raman test to monitor the appearance change of soft carbon on a macroscopic scale. As shown in Fig. S6, no distinct change could be observed for SC-800, while some scattered bright-gold domains are visible in SC-1400 when discharged to 0 V. By contrast, the gold-colored zones grow larger in SC-2000 and become significantly noticeable in SC-2800. Noteworthy is that prior to the emerging of gold domains, blue zones turn up in SC-2000 and SC-2800. This accords well with the previous research [36,41] as stage II GICs exhibit blue color, and the stage I GICs usually display gold color. Therefore, the area of gold domains in soft carbon at 0 V is a reliable indicator showing the proportion of intercalation reaction to form the stage I GICs.

Based on the above discussion, two main K ion storage mechanisms in soft carbon were thus confirmed: i) K ions adsorption on the isolated graphene layers and defect sites; ii) formation of GICs via K ions intercalation into graphitic domains. As depicted

in Fig. 3e, with a large interlayer spacing, abundant defects, and scarce graphitic structure, the K storage in SC-800 abides by the first mechanism. At another extremity, the graphitic soft carbon (SC-2800) mainly follows the second mechanism while SC-1400 and SC-2000 with combined turbostratic and graphitic structures keep to both. The proportion of GICs formation could be qualitatively visualized by comparing the color of the sample at 0V, but a quantitative analysis is expected to shed insights into how the structural stability is affected by the two reaction pathways.

3.3 Performance and stabilities of various active sites

In order to distinguish the capacity contribution from the two charge storage mechanisms, a cyclic voltammetric rate scanning method developed by Dunn et al. [42] was used. Adsorption of K ions is characteristic of a capacitive behavior, whose current intensity at certain potential is proportional to the scan rate, while the intercalation is a diffusion-limited process, for which the corresponding current is proportional to the square root of scan rate. Based on the simulation, it reveals that the contribution by the capacitive process is brought down from 78% for SC-800 to 64% for SC-1400, 37% for SC-2000 and 27% for SC-2800 (Fig. 4a, S7, S8) under the scan rate of 0.5 $mV \cdot s^{-1}$. The observation agrees well with the in-situ Raman results. Intercalation reaction becomes dominant in high-temperature treated soft carbon. Kinetics studies by GITT methods (Fig. 4b, details in S9, S10) indicated that the diffusion coefficients of the four soft carbons are comparable above the K ion intercalation potential of around 0.33 V. In contrast, it shows a sudden decline by orders of magnitude at potentials below 0.3 V for SC-2000 and SC-2800, confirming the sluggish ion migration in graphitic structure upon intercalation. To further probe the structure-related electrochemical behavior of soft carbon in PIBs, rate and galvanostatic cycling tests were conducted. With a pure turbostratic structure and large interlayer distance, SC-800 exhibits the best rate

capability (Fig. 4c). In comparison, with the involvement of intercalation reaction, the rate performance will be undermined to a certain degree depending on the proportion of graphitic domains. For the long-term cycling (Fig. 4d), a capacity retention of 61%, 75%, 62.5%, 83% (compared with the capacity of the 2nd cycle) after 100 cycles is obtained for SC-800, SC-1400, SC-2000 and SC-2800, respectively. Benefitted from the high initial capacity, SC-1400 possesses the highest capacity of 194 mAh·g^{-1} at the 100th cycle among all. It seems that the introduction of graphitic domains might help enhance the cyclic stability of soft carbon, although the intercalation would induce large expansion in the layer distance. An exception is SC-2000, which shows fast capacity degradation, suggesting distinct structural change.

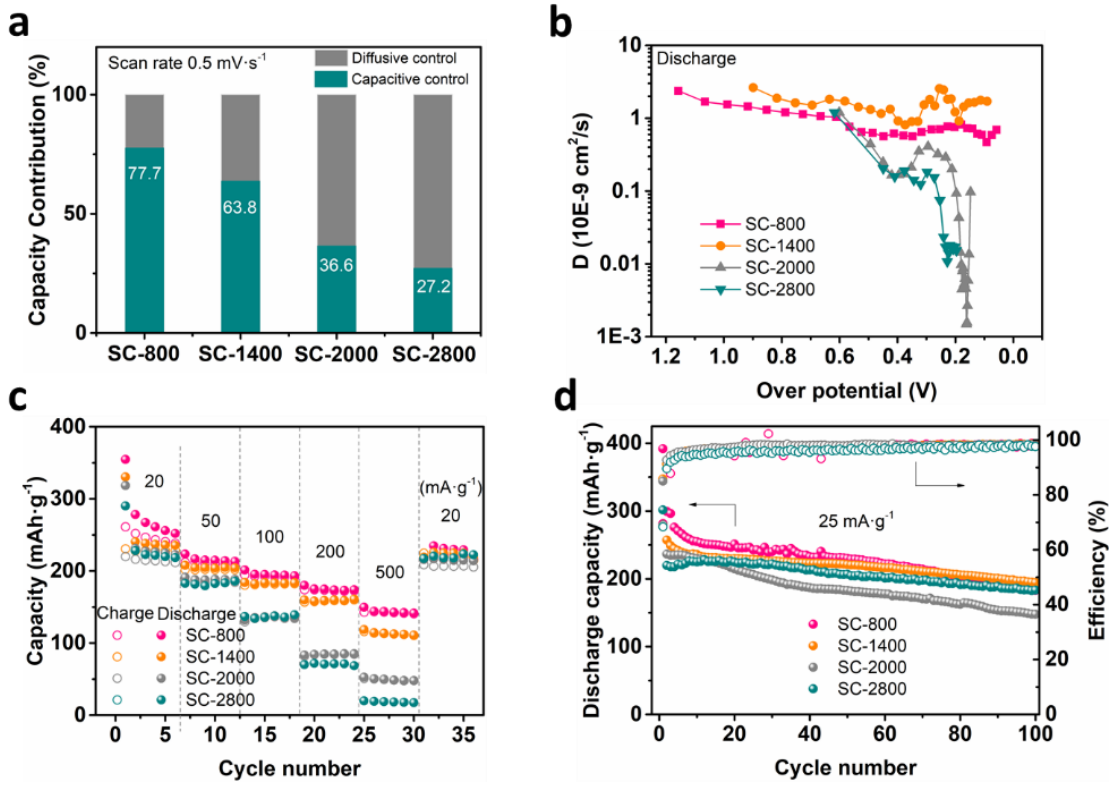

Fig. 4. (a) capacity contribution by capacitive behavior under the scan rate of 0.5 mV·s^{-1}; (b) diffusion coefficient deduced by GITT method; (c) rate capability and (d) cycling performance for SC-800, SC-1400, SC-2000 and SC-2800.

To examine the structural integrity, the cycled electrodes were characterized by

Raman and XRD. Raman spectra in Fig. 5a indicates that the degree of disorder in all samples rises after cycling, with the increasing of I_D/I_G ratios. The significant increase observed in SC-2000 and SC-2800 should be ascribed to the shrinkage of the in-plane crystallite size. XRD patterns for SC-800 and SC-1400 (Fig. 5b) indicate (002) peak diminish after cycles, along with the expansion of the interlayer distance to around 4.0 ~ 4.5 Å and 3.9 ~ 4.4 Å as characterized by TEM (Fig. S11), respectively. The deformation of carbon structure partly accounts for the capacity decay for SC-800 and SC-1400 upon cycling. Noteworthy such structural deteriorations could be largely inhibited through building robust solid electrolyte interphase (SEI), as widely adopted in alloy anodes [xx]. The SC-1400 was tested under an ether-based electrolyte, namely 1.0 M KFSI in EGDE, to demonstrate the concept. A capacity of 188 $mAh \cdot g^{-1}$ could be retained after 200 cycles at 200 $mA \cdot g^{-1}$ without any capacity loss (Fig. Sxx).

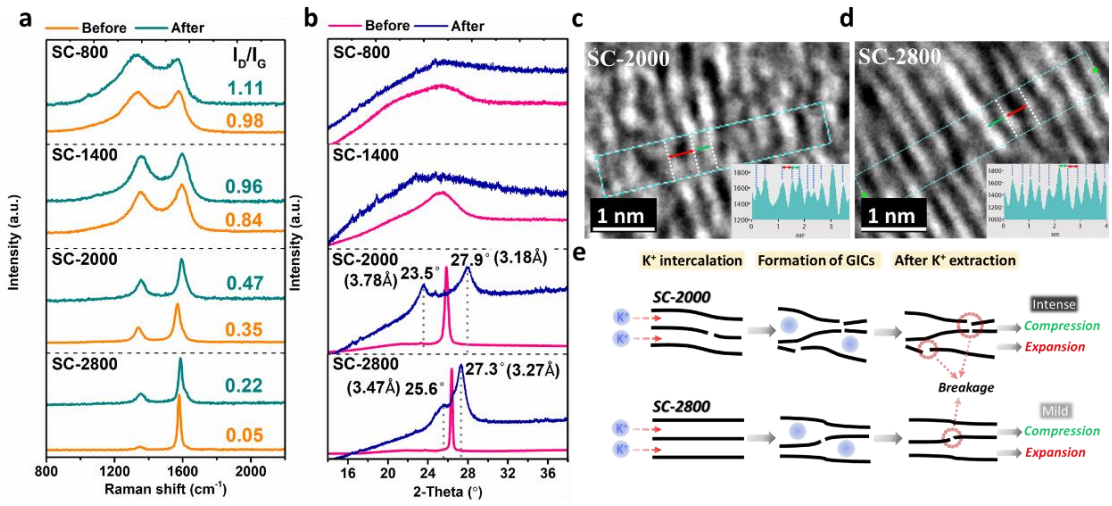

Fig. 5. Comparison of (a) XRD patterns (b) Raman spectra of SC-800, SC-1400, SC-2000 and SC-2800 before and after 100 cycles; HR-TEM images of (c) SC-2000 and (d) SC-2800 after 100 cycles with the insets showing the structural distortion by measurement of interlayer spacings; (e) schematic illustration of the structure deformation mechanisms of SC-2000 and SC-2800 upon K ion intercalation.

For SC-2000 and SC-2800, the (002) peak splits into two sub-peaks with one located at a higher degree and another at a lower degree. The resulting interlayer spacings were calculated to be 3.18 Å (27.9°), 3.78 Å (23.5°) for SC-2000 and 3.27 Å (27.3°), 3.47 Å (25.6°) for SC-2800 by Bragg's law, which is in accordance with the d-spacings measured in TEM images (Fig. S11). Besides that, more details could be found in HR-TEM images. As shown in Fig. 5c, the graphene layers in SC-2000 display severe deformation reflecting in the expansion of specific spaces and the shrinkage of the adjacent areas. The origin of this structure change may lie in the curved graphitic layers with slightly different orientations between neighbor regions in SC-2000, which causes inhomogeneous intercalation exacerbating the structural distortion, as indicated by the non-uniformity of the interlayer spacings shown in the inset of Fig. 5c. Such deformation should, therefore, account for its capacity loss as the compressed areas may no longer act as active sites for K ion storage. It also explains the deviation from regular intercalation pathways in Raman spectra (Fig. 3c). By contrast, this distortion phenomenon is relatively mild in SC-2800 (Fig. 5d and inset). For the highly graphitic structure, alternate expansion/contraction may partly offset the internal stress. Thus the total volume change would not be as severe as that in the quasi-graphitic structure of SC-2000. As a result, SC-2800 shows better cyclic stability. By means of a Raman-assisted method [26], the average graphene layer length (Leq) of SC-2000 and SC-2800 was examined. As presented in Table S7, the Leq of SC-2000 drops from 25.8 to 5.1 nm while that of SC-2800 reduces from 104.2 to 23.4 nm. Noteworthy is that the after-cycle Leq of SC-2800 still maintains at a relatively high value. Although both samples are faced with breaking of graphene layers upon K ion intercalation/extraction, apparently more fractures are generated in SC-2000 after cycles. The relevant structure deformation mechanism is schematically presented in Fig. 5e. Upon K ion intercalation,

the quasi-graphitic structure of SC-2000 tends to undergo severe interlayer expansion and suffer more from the breaking of graphene layers due to its initial short and partly-curved graphene layers. As a result, the structure of SC-2000 displays a higher degree of inhomogeneity while that of SC-2800 shows a higher uniformity.

3.4 Full cell evaluation

Application-wise, it is important to test soft carbon anode in a full-cell scenario. $K_3V_2(PO_4)_2F_3$ was prepared according to our previous work [9] and adopted as a cathode material. It delivers a 2nd cycle discharge capacity of about 96 mAh·g^{-1} within 2.0 ~ 4.6 V (vs. K^+/K) (Fig. S12). The theoretical energy density of the full cells coupling with different soft carbon is calculated based on the voltage profiles and capacities of cathode and anode [46]. It shows the SC-800 would lead to the lowest energy density of 189 Wh·kg^{-1} (all the energy density calculation is based on the mass of cathode and anode), due to its high average potential (Fig. S13 and Table. S8). The utilization of SC-1400, SC2000, and SC-2800 gives similar energy densities of 199, 198, and 198 Wh·kg^{-1}, respectively. Considering the benefits of SC-1400 in the stability and rate capability, a $K_3V_2(PO_4)_2F_3$/SC-1400 full cell was assembled for a proof of concept. By matching the discharge curve of $K_3V_2(PO_4)_2F_3$ with the charge curve of SC-1400 (Fig. 7a), it indicates that an average discharge voltage of around 3.0 V can be obtained and an end-of-discharge voltage of approximately 1.5 V should be appropriate for the full cell. The mass ratio of cathode($K_3V_2(PO_4)_2F_3$)/anode(SC-1400) was controlled at around 2.0 with a slight excess of the anode to avoid the K plating at low potential.

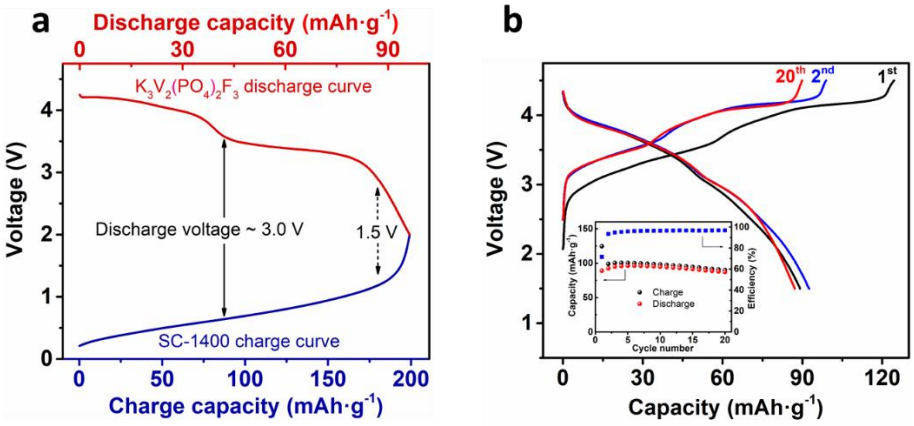

Fig. 7. (a) second cycle discharge ($K_3V_2(PO_4)_2F_3$ in a half cell, upper) and charge (SC-1400 in the half cell, below) curves; (b) voltage profiles of $K_3V_2(PO_4)_2F_3$-SC-1400 full cell within 1.5 - 4.5 V (capacity calculated based on the mass of cathode) and corresponding cycling performance (inset).

As a result, the $K_3V_2(PO_4)_2F_3$/SC-1400 full cell delivers a first cycle charge and discharge capacity of 124.5 and 89.1 $mAh \cdot g^{-1}$, respectively, within 1.5 ~ 4.5 V, corresponding to an initial Coulombic efficiency of 71.6% (Fig. 7b). Upon further cycling, the efficiency gradually rises to above 96% after 5 cycles, along with decent capacity retention at the rate of 0.5 C. The as-assembled full cell demonstrates output energy of 200 $Wh \cdot kg^{-1}$, close to the value obtained in the theoretical calculation. It suggests that soft carbon with a minor degree of graphitization could be a promising anode for K-ion full cells.

4. Conclusion

Soft carbon with different microstructure is prepared by stepwise carbonization of pitch precursor. Through in situ Raman spectroscopy and a series of post-cycle investigations, the K ion storage sites and the corresponding stability upon cycling were revealed:

i) K ion storage in soft carbon is realized either by adsorption on isolated graphene layers and defects or via the intercalation into graphitic domains to form GICs.

ii) Graphitic domains in soft carbon impair its rate capability due to the sluggish kinetics of the intercalation process. However, the increase of the graphitization degree would decrease the average potassiation potential for increasing the energy density in the full cell.

iii) Moderately graphitized soft carbon (the case of SC-1400) delivers the highest reversible capacity with approporiate platueas to achieve attractive energy densities in full cells. The stability could be further enhanced through building a robust SEI.

Acknowledgments

This work is fully supported by the Hong Kong Research Grants Council through the Early Career Scheme (Project No. 25215918). The authors are grateful to Prof. Jianxiao Yang from Hunan University for providing the pitch precursor.

Reference

[1] J.C. Pramudita, D. Sehrawat, D. Goonetilleke, N. Sharma, An Initial Review of the Status of Electrode Materials for Potassium-Ion Batteries, Adv. Energy Mater. 7 (2017) 1–21.

[2] H. Kim, J.C. Kim, M. Bianchini, D.H. Seo, J. Rodriguez-Garcia, G. Ceder, Recent Progress and Perspective in Electrode Materials for K-Ion Batteries, Adv. Energy Mater. 8 (2018) 1–19.

[3] X. Wu, Y. Chen, Z. Xing, C.W.K. Lam, S.S. Pang, W. Zhang, Z. Ju, Advanced Carbon-Based Anodes for Potassium-Ion Batteries, Adv. Energy Mater. 9 (2019) 1–46.

[4] D. Larcher, J.M. Tarascon, Towards greener and more sustainable batteries for electrical energy storage, Nat. Chem. 7 (2015) 19–29.

[5] X. Wu, D.P. Leonard, X. Ji, Emerging Non-Aqueous Potassium-Ion Batteries: Challenges and Opportunities, Chem. Mater. 29 (2017) 5031–5042.

[6] H. Tan, X. Lin, J. Huang, J. Huang, M. Shi, X. Du, B. Zhang, The underestimated charge storage capability of carbon cathodes for advanced alkali metal-ion capacitors, Nanoscale. 11 (2019) 11445–11450.

[7] C. Vaalma, G.A. Giffin, D. Buchholz, S. Passerini, Non-Aqueous K-Ion Battery Based on Layered $K_{0.3}MnO_2$ and Hard Carbon/Carbon Black, J. Electrochem. Soc. 163 (2016) A1295–A1299.

[8] L. Xue, Y. Li, H. Gao, W. Zhou, X. Lü, W. Kaveevivitchai, A. Manthiram, J.B. Goodenough, Low-Cost High-Energy Potassium Cathode, J. Am. Chem. Soc. 139 (2017) 2164–2167.

[9] X. Lin, J. Huang, H. Tan, J. Huang, B. Zhang, $K_3V_2(PO_4)_2F_3$ as a robust cathode for potassium-ion batteries, Energy Storage Mater. 16 (2019) 97–101.

[10] H. Kim, D.H. Seo, M. Bianchini, R.J. Clément, H. Kim, J.C. Kim, Y. Tian, T. Shi, W.S. Yoon, G. Ceder, A New Strategy for High-Voltage Cathodes for K-Ion Batteries: Stoichiometric $KVPO_4F$, Adv. Energy Mater. 8 (2018) 1–12.

[11] L. Wang, J. Yang, J. Li, T. Chen, S. Chen, Z. Wu, J. Qiu, B. Wang, P. Gao, X. Niu, H. Li, Graphite as a potassium ion battery anode in carbonate-based electrolyte and ether-based electrolyte, J. Power Sources. 409 (2019) 24–30.

[12] J. Zhao, X. Zou, Y. Zhu, Y. Xu, C. Wang, Electrochemical Intercalation of Potassium into Graphite, Adv. Funct. Mater. 26 (2016) 8103–8110.

[13] S. Komaba, T. Hasegawa, M. Dahbi, K. Kubota, Potassium intercalation into graphite to realize high-voltage/high-power potassium-ion batteries and potassium-ion capacitors, Electrochem. Commun. 60 (2015) 172–175.

[14] Z. Xing, Y. Qi, Z. Jian, X. Ji, Polynanocrystalline Graphite: A New Carbon Anode with Superior Cycling Performance for K-Ion Batteries, ACS Appl. Mater. Interfaces. 9 (2017) 4343–4351.

[15] Y. An, H. Fei, G. Zeng, L. Ci, B. Xi, S. Xiong, J. Feng, Commercial expanded graphite as a low–cost, long-cycling life anode for potassium–ion batteries with conventional carbonate electrolyte, J. Power Sources. 378 (2018) 66–72.

[16] Z. Zhang, B. Jia, L. Liu, Y. Zhao, H. Wu, M. Qin, K. Han, W.A. Wang, K. Xi, L. Zhang, G. Qi, X. Qu, R.V. Kumar, Hollow Multihole Carbon Bowls: A Stress-Release Structure Design for High-Stability and High-Volumetric-Capacity Potassium-Ion Batteries, ACS Nano. 13 (2019) 11363–11371.

[17] B. Fan, J. Yan, A. Hu, Z. Liu, W. Li, Y. Li, Y. Xu, Y. Zhang, Q. Tang, X. Chen, J. Liu, High-performance potassium ion capacitors enabled by hierarchical porous, large interlayer spacing, active site rich-nitrogen, sulfur Co-doped carbon, Carbon N. Y. 164 (2020) 1–11.

[18] Q. Liu, F. Han, J. Zhou, Y. Li, L. Chen, F. Zhang, D. Zhou, C. Ye, J. Yang, X. Wu, J. Liu, Boosting the Potassium-Ion Storage Performance in Soft Carbon Anodes by the Synergistic Effect of Optimized Molten Salt Medium and N/S Dual-Doping, ACS Appl. Mater. Interfaces. 12 (2020) 20838–20848.

[19] X. Ren, Q. Zhao, W.D. McCulloch, Y. Wu, MoS_2 as a long-life host material for potassium ion intercalation, Nano Res. 10 (2017) 1313–1321.

[20] J. Zheng, Y. Yang, X. Fan, G. Ji, X. Ji, H. Wang, S. Hou, M.R. Zachariah, C. Wang, Extremely stable antimony-carbon composite anodes for potassium-ion batteries, Energy Environ. Sci. 12 (2019) 615–623.

[21] J. Huang, X. Lin, H. Tan, B. Zhang, Bismuth Microparticles as Advanced Anodes for Potassium-Ion Battery, Adv. Energy Mater. 8 (2018) 1–7.

[22] R.A. Adams, A. Varma, V.G. Pol, Carbon Anodes for Nonaqueous Alkali Metal-Ion Batteries and Their Thermal Safety Aspects, Adv. Energy Mater. 9 (2019).

[23] Z. Jian, W. Luo, X. Ji, Carbon Electrodes for K-Ion Batteries, J. Am. Chem. Soc. 137 (2015) 11566–11569.

[24] Z. Jian, S. Hwang, Z. Li, A.S. Hernandez, X. Wang, Z. Xing, D. Su, X. Ji, Hard–Soft Composite Carbon as a Long-Cycling and High-Rate Anode for Potassium-Ion Batteries, Adv. Funct. Mater. 27 (2017) 1–6.

[25] Y. Liu, Y.X. Lu, Y.S. Xu, Q.S. Meng, J.C. Gao, Y.G. Sun, Y.S. Hu, B.B. Chang, C.T. Liu, A.M. Cao, Pitch-Derived Soft Carbon as Stable Anode Material for Potassium Ion Batteries, Adv. Mater. 32 (2020) 1–8.

[26] X. Wang, K. Han, D. Qin, Q. Li, C. Wang, C. Niu, L. Mai, Polycrystalline soft carbon semi-hollow microrods as anode for advanced K-ion full batteries, Nanoscale. 9 (2017) 18216–18222.

[27] N. Xiao, X. Zhang, C. Liu, Y. Wang, H. Li, J. Qiu, Coal-based carbon anodes for high-performance potassium-ion batteries, Carbon N. Y. (2019).

[28] Z. Ju, P. Li, G. Ma, Z. Xing, Q. Zhuang, Y. Qian, Few layer nitrogen-doped graphene with highly reversible potassium storage, Energy Storage Mater. 11 (2018) 38–46.

[29] W. (Alex) Wang, H. Huang, B. Wang, C. Qian, P. Li, J. Zhou, Z. Liang, C. Yang, S. Guo, A new dual-ion battery based on amorphous carbon, Sci. Bull. 64 (2019) 1634–1642.

[30] W. Wang, J. Zhou, Z. Wang, L. Zhao, P. Li, Y. Yang, C. Yang, H. Huang, S.

Guo, Short-Range Order in Mesoporous Carbon Boosts Potassium-Ion Battery Performance, Adv. Energy Mater. 8 (2018) 1–8.

[31] N. Larouche, B.L. Stansfield, Classifying nanostructured carbons using graphitic indices derived from Raman spectra, Carbon N. Y. 48 (2010) 620–629.

[32] J. Maire, J. Mering, Chemistry and physics of carbon, Dekker, NY. 6 (1970) 125.

[33] F. Aune, W. Brockner, H.A. Øte, X-ray characterization of cathode carbon materials, Carbon N. Y. 30 (1992) 1001–1005.

[34] X. Lin, J. Huang, B. Zhang, Correlation between the microstructure of carbon materials and their potassium ion storage performance, Carbon N. Y. 143 (2019) 138–146.

[35] C. Sole, N.E. Drewett, L.J. Hardwick, Insitu Raman study of lithium-ion intercalation into microcrystalline graphite, Faraday Discuss. 172 (2014) 223–237.

[36] J.C. Chacón-Torres, L. Wirtz, T. Pichler, Raman spectroscopy of graphite intercalation compounds: Charge transfer, strain, and electron-phonon coupling in graphene layers, Phys. Status Solidi Basic Res. 251 (2014) 2337–2355.

[37] K. Share, A.P. Cohn, R.E. Carter, C.L. Pint, Mechanism of potassium ion intercalation staging in few layered graphene from in situ Raman spectroscopy, Nanoscale. 8 (2016) 16435–16439.

[38] J.C. Chacon-torres, L. Wirtz, T. Pichler, Manifestation of Charged and Strained Graphene Layers in the Raman Response of Graphite Intercalation Compounds Manifestation of Charged and Strained Graphene Layers in the Raman Response of Graphite Intercalation Compounds, (2013) 9249–9259.

[39] J. Liu, T. Yin, B. Tian, B. Zhang, C. Qian, Z. Wang, L. Zhang, P. Liang, Z. Chen, J. Yan, X. Fan, J. Lin, X. Chen, Y. Huang, K.P. Loh, Z.X. Shen, Unraveling the Potassium Storage Mechanism in Graphite Foam, Adv. Energy Mater. 1900579 (2019) 1–11.

[40] W. Luo, J. Wan, B. Ozdemir, W. Bao, Y. Chen, J. Dai, H. Lin, Y. Xu, F. Gu, V. Barone, L. Hu, Potassium Ion Batteries with Graphitic Materials, Nano Lett. 15 (2015) 7671–7677.

[41] T. Ohzuku, Formation of Lithium-Graphite Intercalation Compounds in Nonaqueous Electrolytes and Their Application as a Negative Electrode for a Lithium Ion (Shuttlecock) Cell, J. Electrochem. Soc. 140 (2006) 2490.

[42] J. Wang, J. Polleux, J. Lim, B. Dunn, Pseudocapacitive contributions to electrochemical energy storage in TiO_2 (anatase) nanoparticles, J. Phys. Chem. C. 111 (2007) 14925–14931.

[43] J.Q. Huang, X. Guo, J. Huang, H. Tan, X. Du, Y. Zhu, B. Zhang, Critical roles of microstructure and interphase on the stability of microsized germanium anode, J. Power Sources. 481 (2021) 228916.

[44] L. Fan, S. Chen, R. Ma, J. Wang, L. Wang, Q. Zhang, E. Zhang, Z. Liu, B. Lu, Ultrastable Potassium Storage Performance Realized by Highly Effective Solid Electrolyte Interphase Layer, Small. 14 (2018) 1–8.

[45] H. Tan, X. Du, R. Zhou, Z. Hou, B. Zhang, Rational design of microstructure and interphase enables high-capacity and long-life carbon anodes for potassium ion batteries, Carbon N. Y. 176 (2021) 383–389.

[46] R. Dugas, B. Zhang, P. Rozier, J.M. Tarascon, Optimization of Na-Ion Battery Systems Based on Polyanionic or Layered Positive Electrodes and Carbon Anodes, J. Electrochem. Soc. 163 (2016) A867–A874.